

# bradscholars

## Aligned electrospun cellulose scaffolds coated with rhBMP-2 for both in vitro and in vivo bone tissue engineering

Item Type	Article
Authors	Zhang, X.;Wang, C.;Liao, M.;Dai, L.;Tang, Y.;Zhang, H.;Coates, Philip;Sefat, Farshid;Zheng, L.;Song, J.;Zheng, Z.;Zhao, D.;Yang, M.;Zhang, W.;Ji, P.
Citation	Zhang X, Wang C, Liao M et al (2019) Aligned electrospun cellulose scaffolds coated with rhBMP-2 for both in vitro and in vivo bone tissue engineering. Carbohydrate Polymers. 213: 27-38.
DOI	<a href="https://doi.org/10.1016/j.carbpol.2019.02.038">https://doi.org/10.1016/j.carbpol.2019.02.038</a>
Rights	© 2019 Elsevier. Reproduced in accordance with the publisher's self-archiving policy. This manuscript version is made available under the CC-BY-NC-ND 4.0 license.
Download date	2026-04-21 11:17:56
Link to Item	<a href="https://bradscholars.brad.ac.uk/handle/10454/16985.2">https://bradscholars.brad.ac.uk/handle/10454/16985.2</a>

---

1           **Aligned Electrospun Cellulose Scaffolds Coated with**  
2           **rhBMP-2 for Both in vitro and in vivo Bone Tissue**  
3           **Engineering**

4  
5   The Authors: Ximu Zhang, Chao Wang, Min Liao, Lina Dai, Yingying Tang,  
6   Hongmei Zhang, Phil Coates, Farshid Sefat, Liwen Zheng, Jinlin Song, Zhuo Zheng,  
7   Dan Zhao, Maobin Yang\*‡, Wei Zhang\*‡, and Ping Ji

8  
9   **Authors' information:**

10   Ximu Zhang<sup>1,2</sup>, ChaoWang<sup>1</sup>, Min Liao<sup>3</sup>, Lina Dai<sup>1</sup>, Yingying Tang<sup>1</sup>, Hongmei Zhang<sup>1</sup>, Phil  
11   Coates<sup>4,5</sup>, Farshid Sefat<sup>4,5</sup>, Liwen Zheng<sup>1</sup>, Jinlin Song<sup>1</sup>, Zhuo Zheng<sup>7</sup>, Dan Zhao<sup>1</sup>, Maobin Yang  
12   \*‡<sup>6</sup>, Wei Zhang \*‡<sup>7</sup> and Ping Ji<sup>1</sup>

13  
14       1, Chongqing Key Laboratory of Oral Disease and Biomedical Sciences & Chongqing  
15       Municipal Key Laboratory of Oral Biomedical Engineering of Higher Education &  
16       Stomatological Hospital of Chongqing Medical University, Chongqing, 401174, China.

17       2, State Key Laboratory of Oral Diseases & National Clinical Research Center for Oral  
18       Diseases & Dept. of Preventive Dentistry, West China Hospital of Stomatology, Sichuan  
19       University, Chengdu, 610041, China.

20       3, Children's Hospital of Chongqing Medical University, Chongqing, 400014, China

21       4, Biomedical and Electrical Engineering Department, School of Engineering, University of  
22       Bradford, Bradford, UK.

23       5, Interdisciplinary Research Centre in Polymer Science & Technology (IRC Polymer),  
24       University of Bradford, Bradford, UK.

25       6, Regenerative Health Research Laboratory, Department of Endodontology, Kornberg  
26       School of Dentistry, Temple University, Philadelphia 19140, USA.

27       7, State Key Laboratory of Polymer Materials Engineering, Polymer Research Institute at  
28       Sichuan University, Chengdu, 610065, China.

29  
30   **AUTHOR INFORMATION**

31       \*: *The corresponding authors*

32   Wei Zhang E-mail: weizhang@scu.edu.cn

33   Maobin Yang E-mail: myang@dental.temple.edu

34   Author Contributions

35   ‡ These authors contributed equally.

36  
37   Notes: The authors declare no competing financial interest.

---

## 39 ABSTRACT

40 Physical properties of scaffolds such as nanofibers and aligned structures have been reported to  
41 exert profound effects on the growth and differentiation of stem cells due to their homing-effect  
42 features and contact guidance. However, the biological function of aligned nanofiber utilized as  
43 bone-scaffold has not been rigorously characterized. In the present study, aligned electrospun  
44 cellulose/CNCs nanocomposite nanofibers (ECCNNs) loaded with bone morphogenic protein-2  
45 (BMP-2) were used for the first time to investigate (1) in vitro osteogenic differentiation of  
46 human mesenchymal stem cells (BMSCs) and (2) in vivo collagen assembly direction and cortical  
47 bone regeneration. Aligned ECCNNs scaffolds loaded with BMP-2 possess good biological  
48 compatibility. The growth orientation of BMSCs followed the underlying aligned nanofibers  
49 morphology, accompanied with increased alizarin red stain, ALP activity and calcium content in  
50 vitro while, a rabbit calvaria bone defect model was used in an in vivo study.

51 **KEYWORDS:** Electrospinning; cellulose; cellulose nanocrystals; aligned nanofibers; collagen  
52 assembly; cortical bone;

53

## 54 1. INTRODUCTION

55

56 Cellulose, categorized as a linear polysaccharide, represents about 1.5 trillion tons of the total  
57 annual biomass production which has been considered as one of the world's most abundant  
58 natural and renewable resource of raw material for the increasing demand of environmental-  
59 friendly and biocompatible products (Ma, Qing, Li, Zhu, Fu & Sun, 2013). Harvesting  
60 nanostructure from natural, sustainable, and earth-abundant raw materials is one of the goals in  
61 the next decades. Recently, the production of nanocellulose biomaterials has received increasing  
62 attention due to their high strength and stiffness combined with small size, low density,  
63 renewability and biodegradability (O'Donnell, Okkelman, Timashev, Gromovykh, Papkovsky &  
64 Dmitriev, 2018). Particularly, the low water solubility and hydrophilicity of cellulose allow for  
65 good control over scaffold fabrication and design (Nada, Abdellatif, Ali, Abdelazeem, Soliman &  
66 Abou-Zeid, 2018). Cellulose-based biomaterials applying in vivo have demonstrated only  
67 negligible inflammatory response reactions and good biocompatibility.

68

69 During the past decade, electrospinning (Zong et al., 2018, Moztarzadeh, 2018, Sefat, 2018a,  
70 Tariverdian, 2018, Sefat, 2018b, Urbanska, 2018, Raja, 2018) has emerged as a promising tool in  
71 tissue engineering because it is easy to produce fibrous structures with diameters ranging from  
72 dozens of nanometers to a few hundred nanometers (Zarrintaj, 2018, Sefat, 2016, Mahjour,  
73 2016), and some physical properties such as fiber alignment and fiber diameter can be precisely  
74 controlled by changing the spinning parameters (Kishan & Cosgriff-Hernandez, 2017, Sefat,  
75 2015). The thin, continuous polymer fibers generated by electrospinning have micro to  
76 nanoscale (<100nm) topography and high porosity (>90%), which is similar to the natural  
77 extracellular matrix (ECM), promoting cellular interactions, guiding cell growth and resulting in  
78 new tissue formation (Yang, Li, He, Ma, Ni & Zhou, 2018). However, electrospun nonwoven  
79 nanofibers usually exhibit poor mechanical strength, representing one of the limitations for the  
80 materials (Sehaqui, Morimune, Nishino & Berglund, 2012). In 2006, Thomas et al (Thomas, Jose,  
81 Chowdhury, Sullivan, Dean & Vohra, 2006) reported the scaffold of electrospun  
82 polycaprolactone (PCL) nanofibers could achieve a high degree of alignment and orientation  
83 when gathered on a fast rotating drum, leading to several-fold increase of the mechanical

---

84 strength along the fiber orientation direction (Raja, 2018).

85 Numerous polymer nanofibers have been fabricated using electrospinning, but electrospun  
86 nanofibers from native cellulose has rarely been reported mainly because cellulose cannot be  
87 directly dissolved in common solvents owing to its high crystallinity enhanced by tremendous  
88 hydrogen bonding network (Wake, Patrick & Mikos, 1994; Wang, Zhang, Zhang, Li, Yu & Lin,  
89 2013). Alternatively, most researches on cellulose electrospinning are based on cellulose  
90 derivatives (Du & Hsieh, 2009; Frey, 2008) and the resultant electrospun fibers are usually very  
91 weak in tensile strength ( $<1$  MPa (Suwanton, Opanasopit, Ruktanonchai & Supaphol, 2007)).  
92 There are limited kinds of solvents that can dissolve cellulose (Jayaramudu, Reddy, Varaprasad,  
93 Sadiku, Sinha Ray & Varada Rajulu, 2013) and so far, only a few of them, namely, N-methyl-  
94 morpholine N-oxide solution/water (NMMO/H<sub>2</sub>O), lithium chloride/dimethyl acetamide  
95 (LiCl/DMAc) and ionic liquids, have been successfully applied for electrospinning of native  
96 cellulose mainly due to the dielectric requirements of this technique (Magalhaes, Cao & Lucia,  
97 2009).

98

99 To address the weak strength of electrospun nanofibers, some stiff nanoparticles have been  
100 blended into the solutions for electrospinning. Cellulose nanocrystals (CNCs) with cellulose I  
101 crystal structure have attracted considerable attention in the nanocomposite field (He et al.,  
102 2014). The theoretical Young's modulus for ideal CNCs is estimated to be 167.5 GPa and elastic  
103 moduli of CNCs from tunicate and cotton have been experimentally confirmed to be up to 105  
104 and 143 GPa, respectively (Podsiadlo, Choi, Shim, Lee, Cuddihy & Kotov, 2005). These excellent  
105 mechanical properties have made CNCs very promising as an effective reinforcement for  
106 polymer nanocomposites (He et al., 2014). Additionally, a hybrid of nanoparticles and  
107 biomaterials sometimes provides extra effects for tissue engineering applications (Bertrand,  
108 Grenier & Mahmoudi, 2017; Zhao, Lu, He, Zhang, Zhang & Zhang, 2015).

109

110 Many researchers have explored nanofiber scaffolds in tissue engineering for the regeneration  
111 of skin (J. Bye, Bullock, Singh, Sefat, Roman & Macneil, 2014; Mahjour, Fu, Yang, Fong, Sefat &  
112 Wang, 2015), nerve (Mohamadi et al., 2017; Mohammadi et al., 2018), cornea (Deshpande et al.,  
113 2013, Ortega et al., 2014), cartilage (Daghigh Ahmadi et al., 2018; Raja et al., 2018; Sefat, 2017),  
114 oral (Nejatian et al., 2017), adipose tissue (Amini et al., 2018) and bone (Sefat, Denyer & Youseffi,  
115 2011, 2014). Among them, aligned nanofibers have become a popular platform for in vitro tissue  
116 engineering attempts due to that they structurally mimic native tissue organization (Driscoll, Sun,  
117 Guven, Fourkas & Losert, 2014). Up to date, most studies reported that repairing bone defect by  
118 tissue engineering increased the volume of sponge bone rather than cortical bone, though the  
119 latter is more significant in loading-bearing site or dental implant than the former. Our previous  
120 study (He et al., 2014) has electrospun uniaxially aligned cellulose nanofibers with well oriented  
121 CNCs embedded. This kind of electrospun cellulose/CNCs nanocomposite nanofibers (ECCNNs)  
122 has four main advantages in tissue engineering: 1) The raw material is cellulose coming from  
123 cotton, which is cost effective, 2) provide aligned structure of nanofibers, 3) and biocompatible.  
124 The degradable product of cellulose is glucose, which has no toxicity; and 4) cellulose  
125 nanocrystals (CNCs) remarkably enhance the mechanical strength of the scaffolds. However, the  
126 effect of well-defined geometries from nanofibers of scaffold on in vivo tissue formation,  
127 particularly in bone healing process, has not yet been fully investigated (Murphy, O'Brien, Little  
128 & Schindeler, 2013). In this study, we loaded rhBMP-2, which is capable to promote osteogenic  
129 differentiation, onto the fabricated aligned ECCNNs. The objectives of this study are to test  
130 whether the aligned ECCNNs loaded with BMP-2 could induce aligned calcium nodules in vitro,  
131 as well as to test the mimicking ECM structure to recruit stem cells in vivo and generate aligned  
132 collagen and cortical bone.

---

## 2. Materials and Methods

134

### 2.1 Materials

135

136 Purified cotton (Xuzhou Health Materials Co., Ltd) was used as the raw material. Analytical grade  
137 N, N-dimethylacetamide (DMAc) and lithium chloride (LiCl) were purchased from Chengdu  
138 Kelong Chemical Plant. For cell culture study, Dulbecco's modified eagle's medium (DMEM),  
139 trypsin, fetal bovine serum (FBS), Dulbecco's Modified Eagle's medium (DMEM), Triton-X 100,  
140 F12, 40,6-diamidino-2-phenylindole (DAPI), rhBMP-2 ELISA kit, Masson Trichrome kit, Alkaline  
141 Phosphatase (ALP) Activity kit and antibiotics (100 U/mL penicillin-streptomycin) were purchased  
142 from Sigma Chemical Co. (St. Louis, MO, USA); Alexa-fluor 568 antibodies were purchased from  
143 Invitrogen (Molecular probes, Carlsbad, CA, USA). Fetal bovine and trypsin were purchased from  
144 Gibco BRL (Life Technologies, Grand Island, NY). rhBMP-2 was purchased from Humanzyme  
145 (Chicago, IL). Glutaraldehyde solution (25%, in weight) was obtained from Zhong-shan Fine-  
146 Chem Ltd. (Guangdong, China). MTS assay kit (Promega™ CellTiter 96™ AQueous Nonradioactive  
147 Cell Proliferation Assay Kit, Promega TM G1111) was purchased from Promega Ltd. (Shanghai,  
148 China). Alizarin Red S staining kit and Calcium assay kit were purchased from Kanto Chemical  
149 (Tokyo, Japan). All the other reagents used were of analytical grade and were used without  
150 further purification. Distilled water was used throughout the experiment.

151

### 2.2 Scaffold Fabrication and rhBMP-2 loading

152

153 Aligned and unaligned/random scaffolds were fabricated using the electrospinning technique as  
154 previously reported (He et al., 2014). Briefly, CNCs were prepared following a hydrolysis method  
155 (Podsiadlo, Choi, Shim, Lee, Cuddihy & Kotov, 2005; Podsiadlo et al., 2007). Then the CNCs were  
156 dispersed in DMAc through a solvent exchange process. Cotton was "activated" and then  
157 dissolved in the LiCl/DMAc (8:92 by weight) solution under magnetic stirring to obtain the 2 wt%  
158 cellulose solution. The cellulose/CNCs spinning dope was prepared by mixing the CNCs  
159 suspension with the cellulose solution. A computer controlled automatic electrospinning  
160 equipment (FM-12, Fuyouma Technology Co., Beijing, China) was used to fabricate ECCNNs at 20  
161 kV voltage, 0.03 mL/min flow rate of the solution. A steel rotating collector (6 cm in diameter)  
162 wrapped with aluminum foil was placed 10 cm away from the tip of the nozzle. The tangential  
163 velocity of the rotating collector was set at 300 m/min and 50 m/min to produce the aligned and  
164 random nanofibers, respectively. The rotating collector was partly immersed in a water  
165 coagulation bath to thoroughly remove the solvent from electrospun fibers and produce  
166 dimensionally stable fibers. The obtained nonwovens were subsequently dried under ventilation  
167 and then kept in a desiccator. A 20% loading (in weight) of CNCs was used in this study since it  
168 could increase the tensile strength and elastic modulus of ECCNNs along the fiber alignment  
169 direction by 101.7 and 171.6%, respectively, as we studied before (He et al., 2014).

170

171 To load rhBMP-2 on the ECCNN scaffold, a circular scaffold (diameter = 8 mm) was fixed on  
172 a spin-coating machine with a bovine collagen solution as the delivery vehicle. The rhBMP-2  
173 doses were chosen according to the literature (Filion, Skelly, Huang, Greiner, Ayers & Song,  
174 2017). Briefly, 40  $\mu$ l bovine collagen solution (3 mg/mL) was mixed with 20  $\mu$ l rhBMP-2  
175 solution (5 mg/mL) in a sterile centrifuge tube. For each loading, 20  $\mu$ l of mixed liquid was  
176 added to the center of the scaffolds (4000 rpm, 20s). To load enough rhBMP-2, this process  
177 was repeated for three times (Perikamana et al., 2015). After that, the central 5 $\times$ 5 mm<sup>2</sup>

---

178 square was cut by a sterilized scissors. All the aforementioned procedures were performed  
179 in an aseptic manner and the rhBMP-2 loaded scaffolds were freshly prepared and stored at  
180 4 °C before use.

181

182 The morphologies of the electrospun fibers were observed on a field-emission scanning electron  
183 microscope (SEM, Inspect F50, FEI) at 20 kV. ImageJ software was used for the analysis of  
184 diameter distributions of more than 100 electrospun fibers selected randomly from the SEM  
185 images. The specific surface area and the pore volume were calculated by Brunauer-Emmett-  
186 Teller (BET) and Barrett-Joyner-Halenda (BJH) methods, respectively. The BMP-2 release was  
187 measured by ELISA kit (Simson, Strehin, Lu, Uy & Elisseeff, 2013).

188

### 189 **2.3 Isolation and culture of bone marrow-derived Stem cells** 190 **(BMSCs)**

191 This study was designed in conformity to the ARRIVE (Animal Research: Reporting of In Vivo  
192 Experiments) guidelines and approved by the Ethics Committee of West China School of  
193 Stomatology, Sichuan University (approval number WCCSIRB-D-2015-073), specific pathogen-  
194 free Wistar rats weighing 80-100 g (male) were purchased from the Laboratory Animal Center of  
195 Sichuan University (Chengdu, Sichuan Province, China). The animals were sacrificed by  
196 anesthesia with 5% isoflurane. The femurs and tibias were harvested and the metaphysis on  
197 both sides was removed using a rongeur under sterile conditions. Bone marrow was collected by  
198 flushing the femur and tibia with medium. Following centrifugation at 150 g for 8 min at 25°C,  
199 the cell pellets were mixed thoroughly with DMEM/F12 supplemented with 10% fetal bovine  
200 serum and antibiotics cultured in 5% CO<sub>2</sub> at 37°C. Medium changes were made every 3-4 days.  
201 Sub-confluent cell monolayers were dissociated using 0.25% trypsin and cells were sub-cultured  
202 to passage 2-4 for the following experiments.

203

### 204 **2.4 Cell Seeding, growth and osteo-Differentiation**

205 Generally, scaffolds were cut by a self-made metal punch with 15 mm diameter, which matched  
206 the 24 well cell culture plate (15.6 mm diameter). 100 µl BMSCs suspension at a density of  $1 \times 10^6$   
207 cells/mL was dropped at the center of the scaffold and cultured in cell incubator in 5% CO<sub>2</sub> at  
208 37°C for 4 hours to allow cells adhere to scaffold not to well of culture plate. After that, 1 mL  
209 osteogenic medium (DMEM media supplemented with 300 µM L-ascorbic acid sodium salt, 10  
210 nM dexamethasone, 10 mM β-glycerophosphate, 10% fetal bovine serum, and 1%  
211 penicillin/streptomycin) was added. The culture medium was changed every 2 days.

212

213 Cells growth and viability and distribution among the scaffolds were assessed using the MTS  
214 assay at day 1, 3, 5, 7. After BMSCs were seeded on scaffold in 96 well plate, DMEM containing  
215 antibiotic solution and 10% fetal bovine serum was used. Cell culture medium was changed  
216 every 2 days. At day 1, 3, 5, 7, culture medium containing MTS solution was added followed by  
217 incubation for 4 h at 37°C. And after 3 h incubation, the absorbance at 490 nm was measured  
218 using a spectrophotometer (Shimadzu, Kyoto, Japan).

219

220 Fluorescence stain was also used for observing the growth situation of BMSCs on scaffold. 2 days  
221 culture after seeding, the cell-scaffold complex was washed twice with PBS and fixed using 4%

---

222 paraformaldehyde for 20 min, then permeabilized in PBS containing 10 vol% FBS plus 0.5 vol%  
223 Triton-X 100 for 20 min, and incubated in PBS containing 10 vol% FBS for 30 min. Thereafter,  
224 samples were stained with Alexa-fluor 568 Conjugated Phalloidin for filamentous actin  
225 fluorescence (1:200) and cell nuclei were marked by DAPI staining for nuclei UV-visualization  
226 (1:2000) for 2 h. Subsequently, specimens were thoroughly washed with PBS, and rinsed with  
227 deionized water for 2 min. Finally, specimens were visualized using an Olympus FV1000 confocal  
228 laser scanning microscope (Olympus, Tokyo, Japan) at 460 nm (emission) and the multitrack  
229 images were captured with a 60×/1.35 NA objective.

230

## 231 **2.5 Osteogenic mineralization in vitro**

232 After BMSCs were co-cultured with scaffolds in osteogenic medium, Alkaline Phosphatase (ALP)  
233 Activity Measurement, Calcium assay and Alizarin Red S staining were done to quantitatively  
234 evaluate the osteo-differentiation effect.

235

236 Briefly, after 14 and 21 days of osteogenic differentiation, cultured scaffolds were cut into small  
237 pieces by scissors, sonicated and centrifuged. Supernatant ALP activity at each time-point was  
238 determined with substrate solution (SIGMA FASTTM p-nitrophenyl phosphate and Tris buffer  
239 tablets, Sigma) by spectrophotometer. Absorbance reading was taken at 405 nm. Meantime,  
240 after 14 and 21 days, those electrospun scaffolds were washed in PBS and were used to  
241 determine calcium content. Calcium was extracted with 0.5 mL 5% trichloroacetic acid for 30 min  
242 and calcium content of the supernatant was determined using creso phthalein complex one  
243 (Teco Diagnostics). The absorbance of samples was measured at 575 nm, followed by the  
244 protocol of the kit.

245

246 Alizarin Red S staining of calcium deposits was done to assess the aligned mineralization of cell  
247 layers. It was done following the study described previously (Dadsetan et al., 2015). Briefly, the  
248 samples were collected after 28 days, fixed with 10% formalin solution for 30 min. 1% Alizarin  
249 Red S stain solution (pH 4.3) was added to each well and incubated for 20 min at room  
250 temperature. The alizarin dye was extracted using 300  $\mu$ L 50% acetic acid solution. The plates  
251 were placed onto a rocker for 10 min to allow for complete dissolution of the dye. The solution  
252 was then placed into 1.5 mL Eppendorf tubes and vortexed for 30 s. The slurry was then  
253 centrifuged and supernatant was added to 10% ammonium hydroxide to bring the pH to 4.1.  
254 Triplicates of 100  $\mu$ L were placed into a 96-well plate and the absorbance was read at 405 nm.  
255 After that, scaffolds were rinsed in PBS for another three times and imaged with a microscope.

256

## 257 **2.6 Animal study for bone regeneration in vivo.**

258 After receiving approval from the Ethics Committee of West China School of Stomatology,  
259 Sichuan University (Approval number WCCSIRB-D-2015-073), adult female New Zealand white  
260 rabbits (West China Laboratory Animal Center) of 7 months old weighting 2-2.5 kg (Dashuo  
261 Laboratory Animals Inc, Chengdu China) were used in this study (n=12). All animal surgeries in  
262 this study were conducted in compliance with the Animal Welfare Act, the implementing Animal  
263 Welfare Regulations, and the principles of the Guide for the Care and Use of Laboratory Animals.  
264 To assess the healing potential of the aligned or random scaffolds with rhBMP-2 (50 $\mu$ g/mL), a  
265 5×5 mm square-sized defect was created in each side of the adult New Zealand white rabbit  
266 cranial bone. Scaffolds were cut into 5×5 mm square size and placed into the bone defect area.  
267 After that, soft tissues were closed in three different layers with resorbable 3-0 sutures. The

---

268 rabbits were recovered and survived for 12 weeks. Then the calvarial samples containing the  
269 healed defects were harvested post euthanasia and fixed in 10% formalin.

270

271 Then each specimen was placed on the scanning platform of a Micro-CT ( $\mu$ 80, Skyscan, Kontich,  
272 Belgium). Micro-CT was performed using a model 1076 apparatus operating with an anode  
273 electrical current of 100 kV, 500 mA at a resolution of 6  $\mu$ m. The regions of interest (ROI) that  
274 included the scaffold and bone defect area, around bone were also selected. After scanning,  
275 three-dimensional (3D) models were generated by CTVol (Skyscan), and bone volume and  
276 density in bone defect area were analyzed by the CTAn program (Skyscan), which was also used  
277 to examine the Micro-CT data sets for new bone growth. The volume of interest (VOI) consisted  
278 of the collective sum of all ROI layers over continuous set of cross-sectional image slices. This  
279 represents the regenerated bone only. Further, new bone volume and bone mineral density in  
280 bone defect area was calculated by the phantom and Housefield units [HU]. A bone threshold  
281 value in CT HU was determined between low phantom (0.25) 1089.7966 HU and high phantom  
282 (0.75) 3241.0643 HU (Zhang et al., 2014). Based on this threshold, a distinction between bone  
283 and no bone volume elements can be made. As the volume of ROI corresponds to the volume of  
284 original bone, the amount of bone present within the ROI is considered as the new formed bone.  
285 To create 3D images binary threshold (Gray scale index, bone defect area: 50 $\times$ 50mm) were  
286 selected.

287

288 After Micro CT scanning, samples were immersed in 10% phosphate-buffered formalin,  
289 decalcified with 10% EDTA at pH 7.4 for 3 months at 4 $^{\circ}$ C with a weekly change of solution, then  
290 samples were dehydrated, cleared and subsequently embedded in paraffin. Tissue sections, 4  
291  $\mu$ m in thickness, were cut using a Leica RM 2265 microtome and mounted on glass slides and  
292 subjected to H&E and Masson Trichrome staining. Images of histology were scanned by Virtual  
293 microscopy solutions (Aperio Technologies Co. the U.S) and viewed by Image Scope viewing  
294 software (Leica Biosystems Co. v11.2.0.780).

295

## 296 **2.7 Statistical analysis**

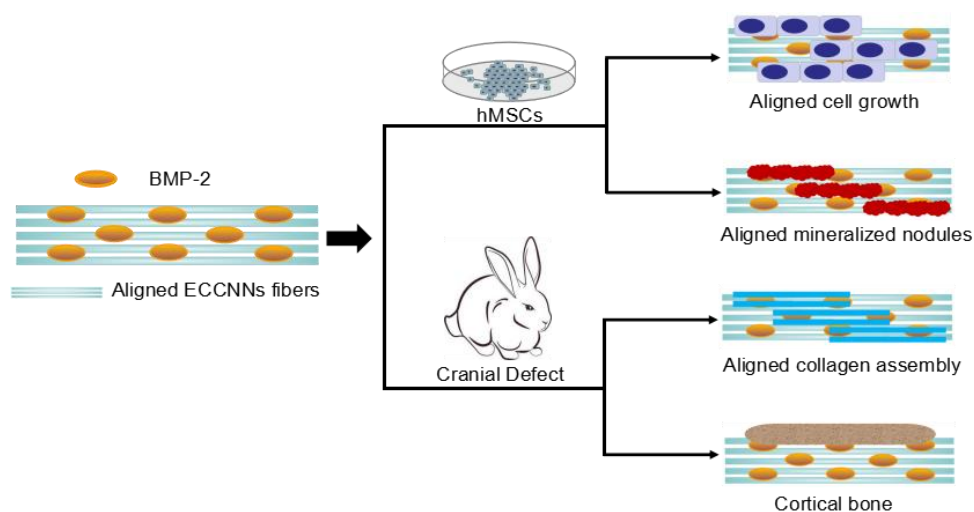
297 Data were collected from triple duplicated samples and all data were represented as mean  $\pm$   
298 standard error of the mean. All results of the control and experimental groups were analyzed  
299 independently. We used one-way ANOVA to examine the differences in the variables among  
300 different experimental conditions.  $p < 0.05$  was considered as statistically significant.

301

302 For the quantification of data, each assay was repeated at least 3 times independently. The  
303 results of the quantitative analyses were expressed as the means  $\pm$  standard error of mean. The  
304 means were compared using one-way analysis of variance (one-way ANOVA) followed by Tukey's  
305 post-hoc assuming equal variances with the SPSS 17 (SPSS, Inc., Chicago, IL, USA). A value of  
306  $P < 0.05$  was considered to indicate a statistically significant difference.

307

### 3. RESULTS AND DISCUSSION



309

310 **Figure 1.** Schematic diagram demonstrating the main experimental procedure in this study

311

312 The main study procedure is presents in Figure 1. In this study, aligned and random/unaligned  
 313 electrospun cellulose nanofibers, enhanced with 20% CNCs were fabricated (He et al., 2014) and  
 314 loaded with BMP-2 (see Methods Section for further details).

315

#### 316 **3.1 Characterization of ECCNNs loaded with BMP-2.**

317 The electrospinning process and the obtained cellulose scaffold were demonstrated in Figure 2.a  
 318 and b. The electrospun nanofiber scaffold appeared in white color and had a relatively smooth  
 319 surface. Figure 2.c, and d presented the SEM images for the random and aligned nanofibers,  
 320 respectively. SEM images clearly showed a difference in morphology for the two types of  
 321 nanofibers. Collecting the fibers at a lower rotation speed (50 m/min) resulted in random  
 322 nanofibers, whereas an irregular nonwoven architecture was revealed in the random sample  
 323 (Figure 2.c), In contrast, a faster rotation speed of the collector (300 m/min) resulted in  
 324 stretching of the fibers in the rotating direction of the collector, which gave highly oriented and  
 325 ordered distribution of individual fibers (Figure 2.d). This finding was consistent with previous  
 326 studies (De Silva et al., 2018; He et al., 2014; Im, Jung, Jang & Kim, 2016).

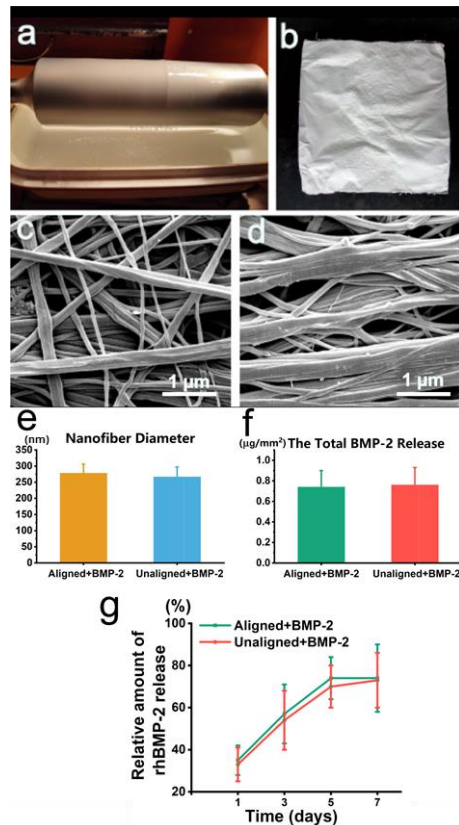
327

328 In our previous study, tensile properties of ECCNNs with a range of CNCs contents were  
 329 measured in directions both along and perpendicular to the fiber orientation (He et al., 2014). In  
 330 this study, 20 wt.% CNCs concentration was selected, which is the maximum concentration for  
 331 electrospinning. The average diameter of nanofibers was  $272.4 \pm 31.64$  nm (Figure 2.e) and there  
 332 was no significant difference in fiber diameter between aligned and random samples. The  
 333 specific surface area and pore volume of the scaffold were determined by nitrogen adsorption  
 334 and calculated with BET and BJH methods, respectively. Due to the nano-dimension of ECCNNs,  
 335 the scaffold exhibited a high surface area of  $12 \text{ m}^2/\text{g}$  and a pore volume of  $0.07 \text{ cm}^3/\text{g}$  with a  
 336 porosity of about 77% (Figure S1 in Supporting Information).

337

338 The total weight of BMP-2 loaded on a  $100 \text{ mm}^2$  scaffold was  $100 \mu\text{g}$ . After 7 days BMP-2

339 releasing test, the total released BMP-2 was detected to be  $0.74 \pm 0.16$  and  $0.76 \pm 0.17$   
 340  $\mu\text{g}/\text{mm}^2$  for aligned and random scaffolds, respectively (Figure 2.f). The relative amount of  
 341 BMP-2 release (%) analyzed by ELISA was shown in Figure 2.g. In view of the area of each  
 342 scaffold ( $25 \text{ mm}^2$ ), the total incorporated amount of rhBMP-2 in each  $5 \times 5 \text{ mm}^2$  sample was  
 343  $25 \mu\text{g}$ . Most BMP-2 was released in the first 5 days. On day 7, the new released BMP-2 was  
 344 hardly detected. (Figure 2.g)



345  
 346 **Figure 2.** Photos of (a) electrospinning process and (b) obtained scaffold. SEM images of (c)  
 347 Aligned and (d) Random nanofibers. (e) Average diameter of BMP-2 coated nanofibers. (f)  
 348 The cumulative amount of BMP-2 released from cellulose electrospun nanofibers in 1 week  
 349 in vitro. (g) The relative amount rhBMP-2 release compared with the total loaded rhBMP-2.  
 350 The concentration of BMP-2 was determined by ELISA. Data are expressed as mean  $\pm$   
 351 standard deviation (SD) of three samples per group.

352

### 353 3.2 The biocompatibility analysis of scaffolds

354 To evaluate the applicability of ECCNNs loaded with BMP-2 for bone regeneration in vitro and in  
 355 vivo, five groups were set in this study. Scaffolds in the five groups was shown in Table 1.

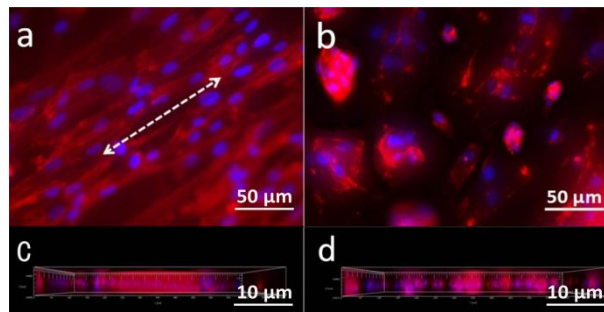
356

357 **Table 1.** Five different groups compared in this study.

358

	Group I	Group II	Group III	Group IV	Group V
Scaffolds	Aligned+BMP-2	Aligned	Random+BMP-2	Random	Empty Control

359



360

361 **Figure 3.** Adhesion and migration of BMSCs in nanofibers. Fluorescence images stained for  
362 F-actin (red) and nuclei (blue) of BMSCs on (a) Aligned and (b) Random nanofibers after 72 h  
363 of culture. After 3D reconstruction of CLSM images, cells could be immersed into (c) Aligned  
364 and (d) Random nanofibers after 72 h of culture.

365

366 BMSCs were isolated and cultured for biocompatibility evaluation. Cell proliferation in the five  
367 groups were investigated by MTS. The proliferation of BMSCs cultured on scaffolds exhibited no  
368 significant difference between each group and empty control on day 1,3,5,7 (Figure.S1). It  
369 suggested all the scaffolds possess great biological compatibility and are suitable for BMSCs  
370 growth and proliferation.

371

372 BMSCs growth situation on scaffolds were analyzed by laser scanning microscopy (CLSM). CLSM  
373 images showed sufficient cell adhesion and widely spread cell morphology on both aligned  
374 (Figure 3.a) and random scaffolds (Figure 3.b) with obvious difference when observed by CLSM.  
375 On aligned scaffold, the cells had spindle shape morphology and stretched along the long axis of  
376 the underlying nanofibers (The direction of white line with double-arrow heads). On random  
377 scaffold, BMSCs were more polygonal in shape and distributed randomly throughout the  
378 nanofibers. After 72 hours of culture, the cells seeded onto the scaffolds surface migrated to the  
379 full depth of the aligned (Figure 3.c) and random (Figure 3.d) scaffold (depth=150 μm). These  
380 results suggested that aligned and random scaffolds have obvious BMSCs guiding potential. The  
381 change in cell adhesion and elongated cellular morphology on nanofibrous scaffolds can be  
382 explained by the classical theory of contact guidance (Jamaiyar et al., 2017). Aligned nanofibers  
383 have recently been explored to employ spatial instruction for different stem cells types, such as  
384 endothelial cells (Chou et al., 2017), neuronal cells (Hyysalo, Ristola, Joki, Honkanen, Vippola &  
385 Narkilahti, 2017), cardiomyocytes (Wanjare, Hou, Nakayama, Kim, Mezak & Abilez, 2017), and  
386 BMSCs (Perikamana et al., 2015). When BMSCs were cultured on aligned poly(L-lactic acid) (PLLA)  
387 nanofibers, the same morphological changes were observed as we reported (Perikamana et al.,  
388 2015).

389

390 Excellent BMSCs adhesion, proliferation and migration on ECCNNs suggest that the hydrophilic  
391 and nanostructured fibers facilitated cell-scaffold interactions. This could be through improved  
392 receptor recognition of fibrillary fibrin, or by increased surface area and roughness, which have  
393 been reported to enhance osteoblasts proliferation and differentiation (Saranya, Saravanan,  
394 Moorthi, Ramyakrishna & Selvamurugan, 2011).

395

396

### 3.3 Mineralization capacity test in vitro

397

398

399

400

401

402

403

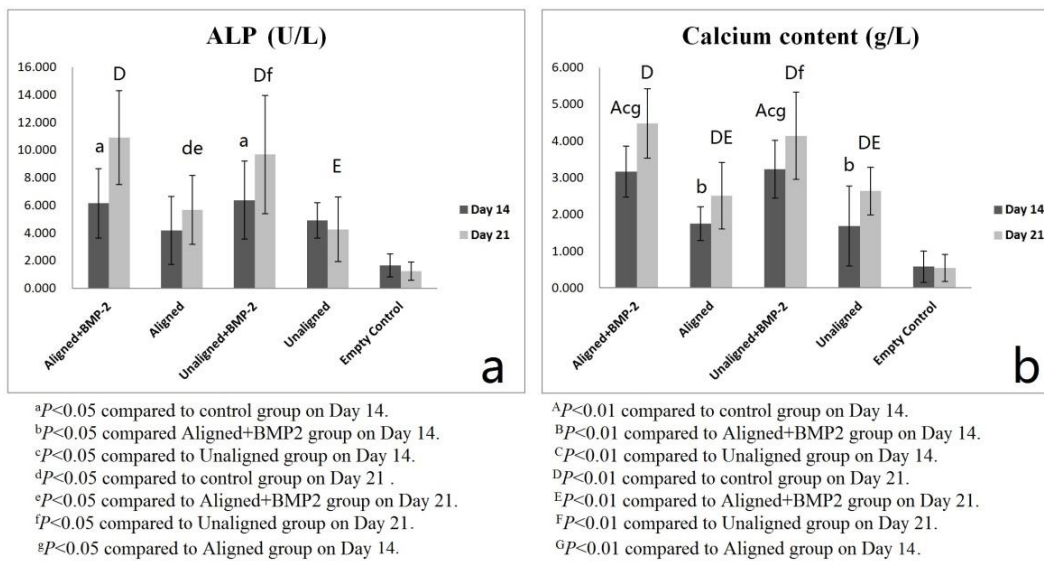
404

405

406

407

Mineralization of BMSCs cultured in osteogenic differentiation medium on different scaffolds was examined using ALP activity and calcium content measurement in each group on day 14 and 21 (Figure 4.a and b). On day 14, ALP activity in the Aligned+ BMP-2 group ( $6.141 \pm 2.503$ ) and Random + BMP-2 group ( $6.362 \pm 2.820$ ) were significantly higher than that in empty control group ( $1.642 \pm 0.835$ ,  $P < 0.05$ ). The difference between empty control and random scaffold group had no significance; On day 21, ALP activity in Aligned+ BMP-2 group ( $10.894 \pm 3.403$ ), Aligned group ( $4.168 \pm 2.462$ ), Random + BMP-2 group ( $9.678 \pm 4.276$ ) and Random group ( $4.915 \pm 1.279$ ) were significantly higher than that in empty control group ( $1.221 \pm 0.657$ ,  $P < 0.01$ ). Adding BMP-2 could significantly increase the ALP activity, no matter in Aligned or Random scaffolds (Figure 4.a).



408

409

410

411

412

413

414

**Figure 4.** (a) ALP activities and (b) Calcium content of BMSCs cultured on five different groups in osteogenic differentiation on day 14 and 21. DMEM+10% fetal calf serum and culture plate was used as empty control. Data are average  $\pm$  standard deviation from 3 samples.

415

416

417

418

419

420

421

422

423

424

425

On day 14, calcium content in the Aligned + BMP-2 group ( $3.16 \pm 0.696$ ) and Random + BMP-2 group ( $3.228 \pm 0.785$ ) were significantly higher than those in empty control group ( $0.574 \pm 0.423$ ,  $P < 0.01$ ), Aligned group ( $1.747 \pm 0.464$ ,  $P < 0.05$ ) and Random group ( $1.685 \pm 1.088$ ,  $P < 0.05$ ). The difference between aligned and random scaffold group with BMP-2 had no significance; On day 21, calcium content in Aligned+ BMP-2 group ( $4.477 \pm 0.947$ ), Aligned group ( $2.509 \pm 0.909$ ), Random + BMP-2 group ( $4.139 \pm 1.19$ ) and Random group ( $2.632 \pm 0.648$ ) were significantly higher than that in empty control group ( $0.541 \pm 0.373$ ,  $P < 0.01$ ). Adding BMP-2 could significantly increase the calcium content, no matter in Aligned or Random scaffolds (Figure 4.b). The ALP and calcium content tests showed that similar levels of osteogenic differentiation of BMSCs could be observed in BMP-2 loading or non-loading groups, irrespective of fiber morphology as well as cell morphology.

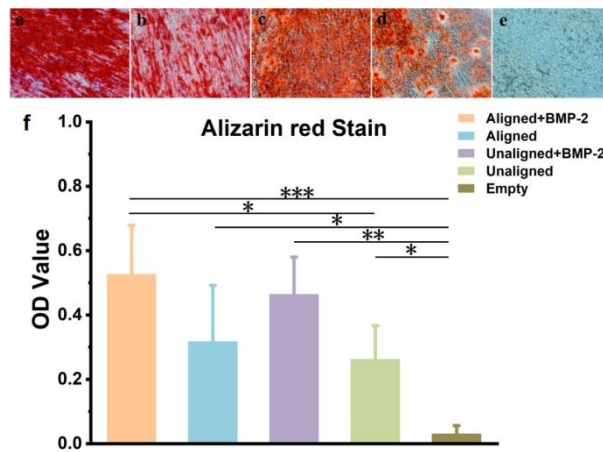
426

427 After 28 days osteogenic differentiation, alizarin red S staining was done (Figure 5.). In contrast,  
428 no staining was observed in empty group. From scaffold with BMP-2 group (Figure 5.a, and 5.c),  
429 Alizarin red S staining was stronger than scaffold without BMP-2 groups (Figure 5.b, and 5.d).  
430 Organized Alizarin red S staining calcium nodules could be seen in aligned scaffold groups (Figure  
431 5.a, and 5.b). Random scaffold groups just showed random alizarin red S staining calcium  
432 nodules (Figure 5.c, and 5.d).

433

434 Alizarin red S staining images showing well-organized mineralized nodules assembly were  
435 observed after 28 days of culture in an osteogenic medium on aligned ECCNNs. Loading BMP-2  
436 increased the quantity of calcium nodules, which followed the same trend of initial cell adhesion.  
437 It is conceivable that cells may prefer to continue their initial cell adhesion behavior and that  
438 ECM secretion can also follow the same pattern, which is consistent with other studies (Liu, Wei,  
439 Zhang, Xu, Yang & Deng, 2013).

440



441

442 **Figure 5.** Alizarin red S staining of BMSCs cultured in osteogenic medium for 28 days on different  
443 scaffolds. (a) Aligned+BMP-2 group, (b) Aligned group, (c) Random+BMP-2 group, (d) Random  
444 group, (e) Empty Control group, (f) Plotted graph represents an Alizarin red Stain based assay of  
445 mineralization. Using culture plate with DMEM and 10% fetal as empty control. (\*,  $P < 0.05$ ,  
446 compared with a line connecting two groups; \*\*,  $P < 0.01$ , compared with a line connecting two  
447 groups).

448

449 In general, different physical factors such as surface topography, stiffness, and shear stress are  
450 influential in osteogenic differentiation of different cells, though osteogenic differentiation on  
451 aligned and random nanofibers is slightly controversial (Perikamana et al., 2015). For example,  
452 Liu et al. claimed that bone marrow mesenchymal stem cells (BMSCs) cultured on random  
453 nanofibers showed increased ALP activity and higher expression of osteogenic genes as  
454 compared to an aligned substrate (Lyu, Huang, Yang & Zhang, 2013). Contrary to these results,  
455 Perikamana et al (Perikamana et al., 2015) demonstrated that aligned nanofibers showed higher  
456 osteogenic differentiation properties than random nanofiber groups did (increase ALP activity  
457 and calcium content). Similarly, higher expression of osteogenic gene markers such as RUNX<sub>2</sub>,  
458 OSX, COL-1, and OCN were observed on aligned nanofibers (Scaglione et al., 2012).

459

460

### 3.4 Bone regeneration test in vivo.

461

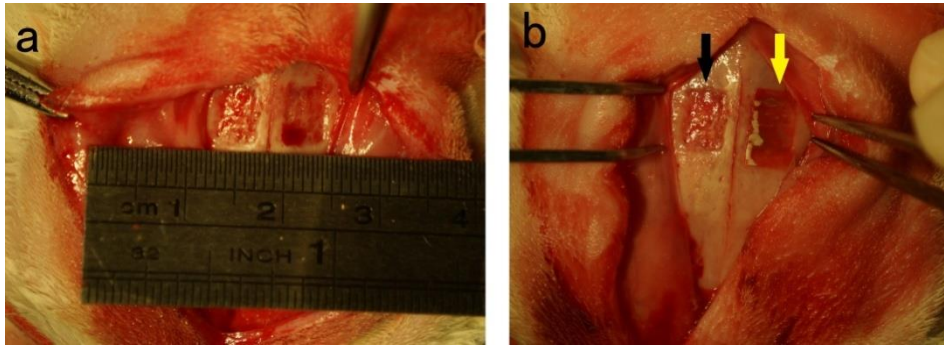
462

463

464

465

466



467

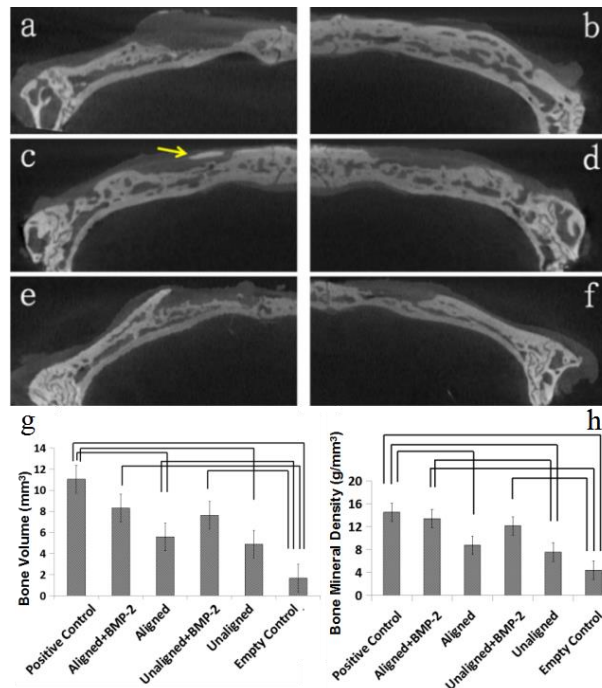
468

469

470

**Figure 6.** Intraoperative image, 5×5 mm square defect was made on each side of rabbit calvaria bone, (a) empty bone defect area (Black arrow) and (b) bone defect area implanted with scaffold (Yellow arrow).

471



472

473

474

475

476

477

478

**Figure 7.** Micro CT images of representative samples from 6 different groups. (a) **Negative** control, (b) **Positive** control, (c) Aligned scaffold with BMP-2, (d) Random scaffold with BMP-2 (e) Aligned scaffold without BMP-2, (f) Random scaffold without BMP-2 (Scale bar: 2 mm), (g) Bone volume and (h) Bone mineral density was quantitatively measured. The difference is significant ( $P<0.05$ ) when compared between two groups with a connecting line.

---

479 Micro CT analysis was carried out for structural and quantitative assessments of new bone  
480 formation and mineralization in the defective site. Two-dimensional (2D) micro-CT images  
481 showed the morphology of cranial defect area. After 12 weeks of surgery, **negative** control  
482 (Figure 7.a) is almost still empty, little new bone formed at the defect site margin. Positive  
483 control (Figure 7.b) is normal cranial micro CT image without surgery. Aligned (Figure 7.c) and  
484 random (Figure 7.d) electrospun cellulose scaffolds loaded with BMP-2 were significantly  
485 different from the **negative** control. More spongy bone was found from the endocardium side,  
486 comparing with the without BMP-2 groups, neither aligned (Figure 7.e) nor random (Figure 7.f)  
487 had much bone formation. Remarkably, some cortical bone could be seen on the skin side in  
488 aligned with BMP-2 group, even it had not shown integrity in the defect side (the yellow arrow in  
489 Figure 7.c).

490

491 Furthermore, the volume of the newly formed bone volume (BV) and bone mineral density  
492 (BMD), the most important parameters of new bone regeneration, were evaluated (Figure 7.g-h).  
493 The values of BV and BMD in aligned group ( $8.63 \text{ mm}^3$ ,  $14.09 \text{ g/cm}^3$ ) and random group ( $7.62$   
494  $\text{mm}^3$ ,  $12.15 \text{ g/cm}^3$ ) loaded with BMP-2 were significantly higher as compared to those for the  
495 defect-only group ( $1.69 \text{ mm}^3$ ,  $4.42 \text{ g/cm}^3$ ,  $P < 0.001$ ), and the difference was not significant when  
496 compared with positive control group ( $10.68 \text{ mm}^3$ ,  $15.01 \text{ g/cm}^3$ ,  $P > 0.05$ ). The BV of aligned group  
497 ( $5.58 \text{ mm}^3$ ) is also significantly higher than that of defect-only group ( $P < 0.05$ ), while no  
498 significant difference was observed in BMD of aligned group ( $8.12 \text{ g/cm}^3$ ,  $P < 0.05$ ), BV and BMD  
499 of unaligned group ( $5.22 \text{ mm}^3$ ,  $7.64 \text{ g/cm}^3$ ) when comparing to the defect-only group ( $P < 0.05$ ).  
500 Furthermore, both BV and BMD were significant lower in aligned and random groups without  
501 BMP-2 loading when compared with positive control group ( $P < 0.05$ ). It means aligned and  
502 unaligned/random scaffolds could induce bone formation in vivo and especially increase the BV  
503 parameter. In addition, loading BMP-2 on ECCNNs could significantly enhance bone formation.

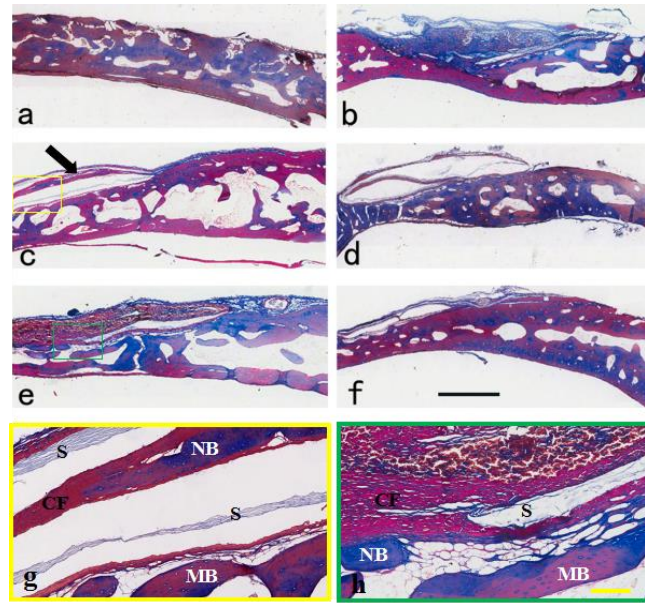
504

505 Masson trichrome staining demonstrated new bone formation and a distribution of regenerated  
506 collagen fibers throughout the bone defect region (Figure 8.a-f). In the aligned ECCNNs with  
507 rhBMP-2 group, the nanofibers were completely covered by newly formed aligned collagen  
508 fibers, which were integrated into the host bone tissues (Figure 8.g). In random ECCNNs with  
509 rhBMP-2 group, the new collagen fiber is also random (Figure 8.f).

510

511 The orientation of the cells was further confirmed by H&E images (Data was shown as  
512 supporting information). In H&E staining images, cell nucleus was stained blue and cytoplasm  
513 was red. In random group, the cell nucleus and the cytoplasm lay randomly; In aligned group,  
514 both the cell nucleus and the cytoplasm followed the same direction (yellow double arrow line),  
515 as parallel to the orientation direction of the nanofibers in scaffold (Figure.S2a). In contrast, the  
516 cells and cell nucleus around the random ECCNNs with BMP-2 scaffold (Figure.S2b) were  
517 distributed randomly, which confirmed the irregular orientation of the nanofibers. Cells cultured  
518 on ECCNNs without BMP-2 have similar image just with less bone formation (data not shown).

519



520

521 **Figure 8.** Masson's Trichrome Stain of representative samples from 6 groups. In these images the  
 522 red stain represents osteoid and blue stain indicates new bone formation (Masson's trichrome  
 523 stain). (a) Positive control, (b) Negative control, (c) aligned scaffold with BMP-2 group, (d)  
 524 aligned scaffold without BMP-2 group, (e) Random scaffold with BMP-2 group, (f) random  
 525 scaffold without BMP-2 group (Scale bar: 2 mm), (g) shows magnified aligned collagen fibers of  
 526 yellow rectangle in (c), (h) shows magnified area of random collagen fibers in green rectangle of  
 527 (e). Labels indicate: Scaffold (S), New bone (NB), Mature bone (MB) and Collagen fibers (CF)  
 528 (Scale bar: 400  $\mu$ m).

529

530 Under Masson's trichrome staining, old bone is stained red, new bone stained in blue and  
 531 collagen fiber stained in red. The positive control (Figure 8.a) is normal cranial sample without  
 532 surgery. The **negative** control (Figure 8.b) is almost still empty, little new bone formatted at the  
 533 defect site margin. Some new sponge bone had regenerated in aligned (Figure 8.c) and random  
 534 (Figure 8.d) electrospun cellulose scaffolds loaded with BMP-2 groups. Even in the aligned  
 535 (Figure 8.e) and random (Figure 8.f) without BMP-2 groups, some new sponge bone has been  
 536 regenerated at the endocardium side. Among these 6 groups, only in ECCNNs with BMP-2 group,  
 537 cortical bone could be seen above the scaffold (Figure 8.c Black arrow).

538

539 Bone is a highly dynamic tissue that is continuously remodeled during its normal growth or  
 540 following injury. Woven bone is initially produced during bone remodeling and is characterized  
 541 by a mechanically weak, disorganized arrangement of collagen fibers. However, during the bone  
 542 remodeling process, woven bone is eventually replaced by regular, parallel aligned collagen  
 543 fibers that form a sheet-like structure called lamellar bone. There is recent evidence that the  
 544 structure of the implanted biomaterials can influence the collagen deposition pattern  
 545 (Perikamana et al., 2015). In this study, we observed that collagen remodeling was strictly  
 546 controlled by the nanofiber architecture. A lamellar-like collagen assembly was found on aligned  
 547 nanofibers, whereas a disorganized, woven-like pattern was observed on the random fibers  
 548 during the same time period. Under natural conditions, bone remodeling is a function of the  
 549 response of the bone to external mechanical loading (Wolf's law) (Molster, Gjerdet, Alho & Bang,  
 550 1983). Besides, for bone tissue engineering, a stronger mechanical strength of the scaffold  
 551 was needed for the cortical bone than sponge bone in vivo (Roohani-Esfahani, Newman &  
 552 Zreiqat, 2016). Though cellulose has the most abundant nature source with excellent

---

553 biocompatibility, electrospun cellulose nanofibers were rarely studied in bone tissue  
554 engineering. In our study, aligned ECCNNs could induce cell growth orderly, mineralize  
555 calcium nodules orderly in vitro, and secret collagen orderly in vivo, which is similar to the  
556 aligned electrospun poly(L-lactic acid) (PLLA) nanofibers in bone regeneration study  
557 (Perikamana et al., 2015). Moreover, aligned ECCNNs exhibited a much stronger mechanical  
558 strength than normal electrospun cellulose nanofibers. This may be the reason that cortical  
559 bone could be seen above the scaffold of aligned ECCNNs loaded with BMP-2, suggesting that  
560 the mechanically strengthened and aligned cellulose nanofibers could influence collagen  
561 remodeling into cortical bone during bone healing. Comparing with a similar study that aligned  
562 collagen was found in aligned electrospun PLLA nanofibers, however, no obvious cortical bone  
563 could be detected. This should be possibly ascribed to the fact that the PLLA scaffold is much  
564 weaker in mechanical strength than aligned ECCNNs scaffold (Perikamana et al., 2015).

565

566 Besides, for tissue engineering applications, scaffolds should have well-controlled pore size and  
567 interconnections (Soliman, Sant, Nichol, Khabiry, Traversa & Khademhosseini, 2011). Increasing  
568 porosity results in greater bone ingrowth and enhanced bone formation, leading to direct  
569 osteogenesis without osteochondral formation as reported by others (Sadowska, Wei, Guo,  
570 Guillem-Marti, Ginebra & Xiao, 2018). However, pore sizes larger than 500 nm are associated  
571 with fibrovascular tissue formation (Smyth, Fournier, Driemeier, Picart, Foster & Bras, 2017; van  
572 Tienen, Heijkants, Buma, de Groot, Pennings & Veth, 2002). The pore size of ECCNNs is about  
573 100-600 nm with a porosity of 77%, which is similar to bone matrix structure (Murphy, O'Brien,  
574 Little & Schindeler, 2013; Wu et al., 2018). The interconnected pore structure of the ECCNNs  
575 scaffolds assists both osteoblasts ingrowth and distribution within the scaffolds and thus may  
576 facilitate angiogenesis and diffusion of nutrients. In addition, the average fiber diameter in each  
577 group was at 250-350 nm (Figure.2e) and is similar to that of collagen fibers in the bone  
578 extracellular microenvironment, which may recruit and induce more endogenous stem cells  
579 from endocranium (He et al., 2014) even without BMP-2 loading. Besides, the nanofiber scaffold  
580 transfers 2D cell culture into 3D culture, more spaces are available to host cell growth as  
581 compared with the culture plate in vitro (Duval et al., 2017). For aligned nanofiber scaffold, the  
582 aligned cell growth pattern makes the cell contact inhibition further reduced (Figure 7.g). (Nuhn,  
583 Perez & Schneider, 2018).

584

585 Finally, we propose a possible mechanism of in vivo collagen matrix assembly guided by aligned  
586 ECCNNs with BMP-2, which involved 5 aspects: 1). Electrospun nanofiber scaffold has a similar  
587 structure to ECM and cellulose is biocompatible, which could induce the "homing effect" of stem  
588 cells and support their attachment; 2) Through contact guidance, aligned nanofibers instructed  
589 endogenous progenitor cells adhesion and growth by the nanofiber morphology; 3) Loading  
590 BMP-2 on scaffold actively turns endogenous progenitor cells into osteoblasts; 4) The  
591 osteoblasts secrete collagen along the direction of cell adhesion (fiber direction), which  
592 subsequently forms the collagen fibril bundles in the direction of deposited collagen molecules;  
593 5) Individual collagen fibrils may undergo directional mineralization, and these mineralized  
594 structures are then assembled together to form an organized structure of bone (cortical bone).

595

## 596 **4. CONCLUSION**

597 The results of the present study suggest that the combination of BMP-2 and aligned ECCNNs  
598 scaffold has great potential for bone regeneration. Aligned cellulose nanofibers could induce  
599 aligned BMSCs growth and mineralized nodules formation in vitro, and assembly aligned

600 collagen and cortical bone formation in vivo. The study provides a basis for future optimization  
601 of electrospun nanofibrous scaffolds for bone tissue engineering applications.

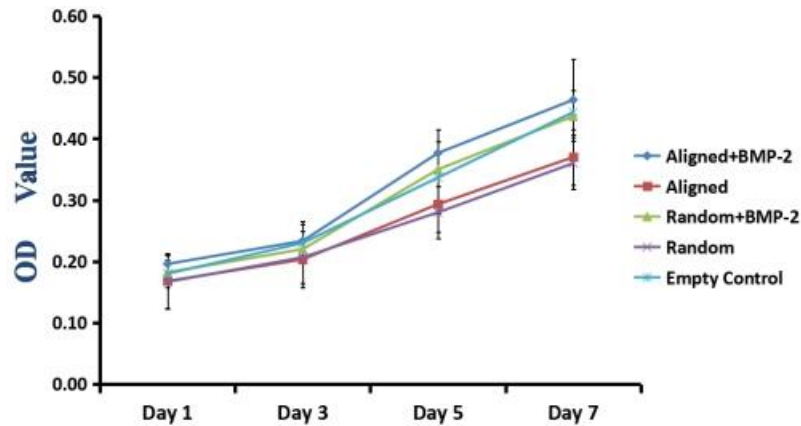
602

## 603 ASSOCIATED CONTENT

604

605 Supporting Information

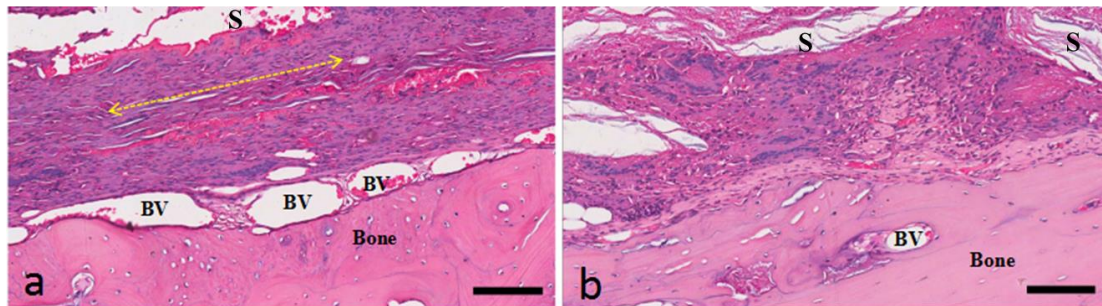
606



607

608 **Figure.S1** Analysis of the proliferation of BMSCs on different group by MTS assay on day 1, 3, 5,  
609 7. Bars represent the means  $\pm$  Sd. There was no significant difference between different  
610 groups at each day. Plastic culture plate was used as Empty Control.

611



612

613 **Figure.S2.** H&E Stain. Aligned and random cells and collagen could be seen in aligned (a) and  
614 random (b) groups. Aligned cellulose Loading BMP-2 gave more new bone formation. BV:  
615 Blood vessel, S: scaffold.

616

## 617 ACKNOWLEDGEMENT

618 This work was supported by Natural Science Foundation of China (NSFC) grants (31500789,  
619 51433006, 51473100, 81870758 and 31871464), Chongqing Yuzhong District science and  
620 technology plan project grants (20170124), Chongqing Research Program of Basic Research  
621 and Frontier Technology (cstc2018jcyjAX0807, cstc2017jcyjBX0019 and cstc2017jcyjAX0020),  
622 Temple University Kornberg School of Dentistry research start-up funds, the RCUK China-UK  
623 Science Bridges Program through the Medical Research Council and the Engineering and

---

624 Physical Sciences Research Council and Program for Innovation Team 1015 Building at  
625 Institutions of Higher Education (No. 1016 CXTDG201602006) funded by the Chongqing  
626 Municipal 1017 Education Commission of China in 2016.

627

628 ***The authors declare no competing financial interest.***

629

## 630 **References:**

631

632 Amini, N., Vouseoghi, N., Alizade, A., Ramezani, S., Joghataei, M. T., Milan, P. B., Mehrabi, S.,  
633 Ababzadeh, S., Sefat, F., & Mozafari, M. (2018). Transplantation of adipose tissue-derived stem cells  
634 into brain through cerebrospinal fluid in rat models: Protocol development and initial outcome data.  
635 *Curr Stem Cell Res Ther.*

636

637 Bertrand, N., Grenier, P., & Mahmoudi, M. (2017). Mechanistic understanding of in vivo protein  
638 corona formation on polymeric nanoparticles and impact on pharmacokinetics. *8(1)*, 777.

639

640 Chou, C. L., Rivera, A. L., Williams, V., Welter, J. F., Mansour, J. M., Drazba, J. A., Sakai, T., & Baskaran,  
641 H. (2017). Micrometer scale guidance of mesenchymal stem cells to form structurally oriented large-  
642 scale tissue engineered cartilage. *Acta Biomater*, *60*, 210-219.

643

644 Dadsetan, M., Guda, T., Runge, M. B., Mijares, D., LeGeros, R. Z., LeGeros, J. P., Silliman, D. T., Lu, L.,  
645 Wenke, J. C., Brown Baer, P. R., & Yaszemski, M. J. (2015). Effect of calcium phosphate coating and  
646 rhBMP-2 on bone regeneration in rabbit calvaria using poly(propylene fumarate) scaffolds. *Acta*  
647 *Biomater*, *18*, 9-20.

648

649 Daghigh Ahmadi, E., Israr Raja, T., Ali Khaghani, S., Fhong Soon, C., Mozafari, M., Youseffi, M., & Sefat,  
650 F. (2018). The role of photonics and natural curing agents of TGF- $\beta$ 1 in treatment of osteoarthritis.  
651 *Materials Today: Proceedings*, *5(7)*, 15540-15549.

652

653 De Silva, R. T., Dissanayake, R. K., Mantilaka, M., Wijesinghe, W., Kaleel, S. S., Premachandra, T. N.,  
654 Weerasinghe, L., Amaratunga, G. A. J., & de Silva, K. M. N. (2018). Drug-Loaded Halloysite Nanotube-  
655 Reinforced Electrospun Alginate-Based Nanofibrous Scaffolds with Sustained Antimicrobial  
656 Protection.

657

658 Deshpande, P., Ramachandran, C., Sefat, F., Mariappan, I., Johnson, C., McKean, R., Hannah, M.,  
659 Sangwan, V. S., Claeyssens, F., Ryan, A. J., & MacNeil, S. (2013). Simplifying corneal surface  
660 regeneration using a biodegradable synthetic membrane and limbal tissue explants. *Biomaterials*,  
661 *34(21)*, 5088-5106.

662

---

663 Driscoll, M. K., Sun, X., Guven, C., Fourkas, J. T., & Losert, W. (2014). Cellular contact guidance  
664 through dynamic sensing of nanotopography. *ACS Nano*, 8(4), 3546-3555.

665 Du, J., & Hsieh, Y.-L. (2009). *Cellulose/chitosan hybrid nanofibers from electrospinning of their ester*  
666 *derivatives*.

667

668 Duval, K., Grover, H., Han, L. H., Mou, Y., Pegoraro, A. F., Fredberg, J., & Chen, Z. (2017). Modeling  
669 Physiological Events in 2D vs. 3D Cell Culture. 32(4), 266-277.

670

671 Filion, T. M., Skelly, J. D., Huang, H., Greiner, D. L., Ayers, D. C., & Song, J. (2017). Impaired  
672 osteogenesis of T1DM bone marrow-derived stromal cells and periosteum-derived cells and their  
673 differential in-vitro responses to growth factor rescue. *Stem Cell Res Ther*, 8(1), 65.

674

675 Frey, M. (2008). *Electrospinning Cellulose and Cellulose Derivatives*.

676

677 He, X., Xiao, Q., Lu, C., Wang, Y., Zhang, X., Zhao, J., Zhang, W., Zhang, X., & Deng, Y. (2014).  
678 Uniaxially aligned electrospun all-cellulose nanocomposite nanofibers reinforced with cellulose  
679 nanocrystals: scaffold for tissue engineering. *Biomacromolecules*, 15(2), 618-627.

680

681 Hyysalo, A., Ristola, M., Joki, T., Honkanen, M., Vippola, M., & Narkilahti, S. (2017). Aligned  
682 Poly(epsilon-caprolactone) Nanofibers Guide the Orientation and Migration of Human Pluripotent  
683 Stem Cell-Derived Neurons, Astrocytes, and Oligodendrocyte Precursor Cells In Vitro. *Macromol*  
684 *Biosci*, 17(7).

685

686 Im, S. H., Jung, Y., Jang, Y., & Kim, S. H. (2016). Poly(L-lactic acid) scaffold with oriented micro-valley  
687 surface and superior properties fabricated by solid-state drawing for blood-contact biomaterials.  
688 *Biofabrication*, 8(4), 045010.

689

690 J. Bye, F., Bullock, A., Singh, R., Sefat, F., Roman, S., & Macneil, S. (2014). *Development of a Basement*  
691 *Membrane Substitute Incorporated Into an Electrospun Scaffold for 3D Skin Tissue Engineering*.

692

693 Jamaiyar, A., Wan, W., Ohanyan, V., Enrick, M., Janota, D., Cumpston, D., Song, H., Stevanov, K., Kolz,  
694 C. L., Hakobyan, T., Dong, F., Newby, B. Z., Chilian, W. M., & Yin, L. (2017). Alignment of inducible  
695 vascular progenitor cells on a micro-bundle scaffold improves cardiac repair following myocardial  
696 infarction. *Basic Res Cardiol*, 112(4), 41.

697

698 Jayaramudu, J., Reddy, G. S., Varaprasad, K., Sadiku, E. R., Sinha Ray, S., & Varada Rajulu, A. (2013).  
699 Preparation and properties of biodegradable films from Sterculia urens short fiber/cellulose green  
700 composites. *Carbohydr Polym*, 93(2), 622-627.

701

702 Kishan, A. P., & Cosgriff-Hernandez, E. M. (2017). Recent advancements in electrospinning design for

---

703 tissue engineering applications: A review. *J Biomed Mater Res A*, 105(10), 2892-2905.

704

705 Liu, W., Wei, Y., Zhang, X., Xu, M., Yang, X., & Deng, X. (2013). Lower extent but similar rhythm of  
706 osteogenic behavior in hBMSCs cultured on nanofibrous scaffolds versus induced with osteogenic  
707 supplement. *ACS Nano*, 7(8), 6928-6938.

708

709 Lyu, S., Huang, C., Yang, H., & Zhang, X. (2013). Electrospun fibers as a scaffolding platform for bone  
710 tissue repair. *J Orthop Res*, 31(9), 1382-1389.

711

712 Ma, M. G., Qing, S. J., Li, S. M., Zhu, J. F., Fu, L. H., & Sun, R. C. (2013). Microwave synthesis of  
713 cellulose/CuO nanocomposites in ionic liquid and its thermal transformation to CuO. *Carbohydr*  
714 *Polym*, 91(1), 162-168.

715

716 Magalhaes, W. L., Cao, X., & Lucia, L. A. (2009). Cellulose nanocrystals/cellulose core-in-shell  
717 nanocomposite assemblies. *Langmuir*, 25(22), 13250-13257.

718

719 Mahjour, S. B., Fu, X., Yang, X., Fong, J., Sefat, F., & Wang, H. (2015). Rapid creation of skin  
720 substitutes from human skin cells and biomimetic nanofibers for acute full-thickness wound repair.  
721 *Burns*, 41(8), 1764-1774.

722

723 Mahjour, S., Sefat, F., Polunin, Y., Wang, L. and Wang, H. (2016) Improved cell infiltration of  
724 electrospun nanofiber mats for layered tissue constructs. *Journal of Biomedical Materials Research*  
725 *Part A*, 104(6), pp.1479-1488.

726

727 Mohamadi, F., Ebrahimi-Barough, S., Nourani, M. R., Mansoori, K., Salehi, M., Alizadeh, A. A.,  
728 Tavangar, S. M., Sefat, F., Sharifi, S., & Ai, J. (2017). Enhanced sciatic nerve regeneration by human  
729 endometrial stem cells in an electrospun poly (epsilon-caprolactone)/collagen/NBG nerve conduit in  
730 rat. *Artif Cells Nanomed Biotechnol*, 1-13.

731

732 Mohammadi, A., Maleki-Jamshid, A., Sanooghi, D., Milan, P. B., Rahmani, A., Sefat, F., Shahpasand, K.,  
733 Soleimani, M., Bakhtiari, M., Belali, R., Faghihi, F., Joghataei, M. T., Perry, G., & Mozafari, M. (2018).  
734 Transplantation of Human Chorion-Derived Cholinergic Progenitor Cells: a Novel Treatment for  
735 Neurological Disorders.

736

737 Molster, A. O., Gjerdet, N. R., Alho, A., & Bang, G. (1983). Fracture healing after rigid intramedullary  
738 nailing in rats. *Acta Orthop Scand*, 54(3), 366-373.

739

740 Murphy, C. M., O'Brien, F. J., Little, D. G., & Schindeler, A. (2013). Cell-scaffold interactions in the  
741 bone tissue engineering triad. *Eur Cell Mater*, 26, 120-132.

742

---

743 Moztarzadeh, S., Mottaghy, K., Sefat, F., Samadikuchaksaraei, A. and Mozafari, M. (2018)  
744 Nanoengineered biomaterials for lung regeneration. *Nanoengineered Biomaterials for Regenerative*  
745 *Medicine*, pp.305-323.

746

747 Nada, A. A., Abdellatif, F. H. H., Ali, E. A., Abdelazeem, R. A., Soliman, A. A. S., & Abou-Zeid, N. Y.  
748 (2018). Cellulose-based click-scaffolds: Synthesis, characterization and biofabrications. *Carbohydr*  
749 *Polym*, 199, 610-618.

750

751 Nejatian, T., Khurshid, Z., Zafar, M. S., Najeeb, S., Zohaib, S., Mazafari, M., Hopkinson, L., & Sefat, F.  
752 (2017). 5 – Dental biocomposites. *Biomaterials for Oral & Dental Tissue Engineering*, 65-84.

753

754 Nuhn, J. A. M., Perez, A. M., & Schneider, I. C. (2018). Contact guidance diversity in rotationally  
755 aligned collagen matrices. *Acta Biomater*, 66, 248-257.

756

757 O'Donnell, N., Okkelman, I. A., Timashev, P., Gromovykh, T. I., Papkovsky, D. B., & Dmitriev, R. I.  
758 (2018). Cellulose-based scaffolds for fluorescence lifetime imaging-assisted tissue engineering. *Acta*  
759 *Biomater*.

760

761 Ortega, Í., Sefat, F., Deshpande, P., Paterson, T., Ramachandran, C., Ryan, A., MacNeil, S. and  
762 Claeysens, F. (2014) Combination of Microstereolithography and Electrospinning to Produce  
763 Membranes Equipped with Niches for Corneal Regeneration. *Journal of Visualized Experiments*, (91).

764

765 Perikamana, S. K., Lee, J., Ahmad, T., Jeong, Y., Kim, D. G., Kim, K., & Shin, H. (2015). Effects of  
766 Immobilized BMP-2 and Nanofiber Morphology on In Vitro Osteogenic Differentiation of hMSCs and  
767 In Vivo Collagen Assembly of Regenerated Bone. *ACS Appl Mater Interfaces*, 7(16), 8798-8808.

768

769 Podsiadlo, P., Choi, S. Y., Shim, B., Lee, J., Cuddihy, M., & Kotov, N. A. (2005). Molecularly engineered  
770 nanocomposites: layer-by-layer assembly of cellulose nanocrystals. *Biomacromolecules*, 6(6), 2914-  
771 2918.

772

773 Podsiadlo, P., Sui, L., Elkasabi, Y., Burgardt, P., Lee, J., Miryala, A., Kusumaatmaja, W., Carman, M. R.,  
774 Shtein, M., Kieffer, J., Lahann, J., & Kotov, N. A. (2007). Layer-by-layer assembled films of cellulose  
775 nanowires with antireflective properties. *Langmuir*, 23(15), 7901-7906.

776

777 Raja, T., Khaghani, S., Zafar, M., Khurshid, Z., Mozafari, M., Youseffi, M. and Sefat, F. (2018) Effect of  
778 TGF- $\beta$ 1 on water retention properties of healthy and osteoarthritic chondrocytes. *Materials Today:*  
779 *Proceedings*, 5(7), pp.15717-15725.

780

---

781 Raja, T., Mozafari, M., Milan, P., Samadikuchaksaraei, A. and Sefat, F. (2018) Nanoengineered  
782 biomaterials for tracheal replacement. *Nanoengineered Biomaterials for Regenerative Medicine*,  
783 pp.285-303.

784

785 Sadowska, J. M., Wei, F., Guo, J., Guillem-Marti, J., Ginebra, M. P., & Xiao, Y. (2018). Effect of nano-  
786 structural properties of biomimetic hydroxyapatite on osteoimmunomodulation. *Biomaterials*, *181*,  
787 318-332.

788

789 Saranya, N., Saravanan, S., Moorthi, A., Ramyakrishna, B., & Selvamurugan, N. (2011). Enhanced  
790 osteoblast adhesion on polymeric nano-scaffolds for bone tissue engineering. *J Biomed Nanotechnol*,  
791 *7*(2), 238-244.

792

793 Scaglione, S., Giannoni, P., Bianchini, P., Sandri, M., Marotta, R., Firpo, G., Valbusa, U., Tampieri, A.,  
794 Diaspro, A., Bianco, P., & Quarto, R. (2012). Order versus Disorder: in vivo bone formation within  
795 osteoconductive scaffolds. *Sci Rep*, *2*, 274.

796

797 Schoolaert, E., Ryckx, P., Geltmeyer, J., Maji, S., Van Steenberge, P. H. M., & D'Hooge D, R. (2017).  
798 Waterborne Electrospinning of Poly(N-isopropylacrylamide) by Control of Environmental Parameters.  
799 *9*(28), 24100-24110.

800

801 Sefat, F. (2017). Fabrication and Characterizations of Hydrogels for Cartilage Repair. *Advances in*  
802 *Tissue Engineering & Regenerative Medicine: Open Access*, *2*(6).

803

804 Sefat, F., Denyer, M. C., & Youseffi, M. (2011). Imaging via widefield surface plasmon resonance  
805 microscope for studying bone cell interactions with micropatterned ECM proteins. *J Microsc*, *241*(3),  
806 282-290.

807

808 Sefat, F., Denyer, M. C., & Youseffi, M. (2014). Effects of different transforming growth factor beta  
809 (TGF-beta) isomers on wound closure of bone cell monolayers. *Cytokine*, *69*(1), 75-86.

810

811 Sefat, F., Raja, T., Zafar, M., Khurshid, Z., Najeeb, S., Zohaib, S., Ahmadi, E., Rahmati, M. and Mozafari,  
812 M. (2018a) Nanoengineered biomaterials for cartilage repair. *Nanoengineered Biomaterials for*  
813 *Regenerative Medicine*, pp.39-71.

814

815 Sefat, F., Raja, T., Moghadam, Z., Milan, P., Samadikuchaksaraei, A. and Mozafari, M. (2018b)  
816 Nanoengineered biomaterials for bladder regeneration. *Nanoengineered Biomaterials for*  
817 *Regenerative Medicine*, pp.459-474.

818

819 Sefat, F., Youseffi, M., Khaghani, S., Soon, C. and Javid, F. (2016) Effect of transforming growth  
820 factor- $\beta$ 3 on mono and multilayer chondrocytes. *Cytokine*, *83*, pp.118-126.

---

821

822 Sefat, F., Khaghani, S., Nejatian, T., Genedy, M., Abdeldayem, A., Moghaddam, Z., Denyer, M. and  
823 Youseffi, M. (2015) Transforming growth factor beta (TGF- $\beta$ ) isomers influence cell detachment of  
824 MG-63 bone cells. *Tissue and Cell*, 47(6), pp.567-574.

825

826 Sehaqui, H., Morimune, S., Nishino, T., & Berglund, L. A. (2012). Stretchable and strong cellulose  
827 nanopaper structures based on polymer-coated nanofiber networks: an alternative to nonwoven  
828 porous membranes from electrospinning. *Biomacromolecules*, 13(11), 3661-3667.

829

830 Simson, J. A., Strehin, I. A., Lu, Q., Uy, M. O., & Elisseeff, J. H. (2013). An adhesive bone marrow  
831 scaffold and bone morphogenetic-2 protein carrier for cartilage tissue engineering.  
832 *Biomacromolecules*, 14(3), 637-643.

833

834 Smyth, M., Fournier, C., Driemeier, C., Picart, C., Foster, E. J., & Bras, J. (2017). Tunable Structural  
835 and Mechanical Properties of Cellulose Nanofiber Substrates in Aqueous Conditions for Stem Cell  
836 Culture. *18(7)*, 2034-2044.

837

838 Soliman, S., Sant, S., Nichol, J. W., Khabiry, M., Traversa, E., & Khademhosseini, A. (2011). Controlling  
839 the porosity of fibrous scaffolds by modulating the fiber diameter and packing density. *J Biomed*  
840 *Mater Res A*, 96(3), 566-574.

841

842 Suwantong, O., Opanasopit, P., Ruktanonchai, U., & Supaphol, P. (2007). *Electrospun cellulose*  
843 *acetate fiber mats containing curcumin and release characteristic of the herbal substance.*

844

845 Tariverdian, T., Zarintaj, P., Milan, P., Saeb, M., Kargozar, S., Sefat, F., Samadikuchaksaraei, A. and  
846 Mozafari, M. (2018) Nanoengineered biomaterials for kidney regeneration. *Nanoengineered*  
847 *Biomaterials for Regenerative Medicine*, pp.325-344.

848

849 Thomas, V., Jose, M. V., Chowdhury, S., Sullivan, J. F., Dean, D. R., & Vohra, Y. K. (2006). Mechano-  
850 morphological studies of aligned nanofibrous scaffolds of polycaprolactone fabricated by  
851 electrospinning. *J Biomater Sci Polym Ed*, 17(9), 969-984.

852

853 Urbanska, A., Sefat, F., Yousaf, S., Kargozar, S., Milan, P. and Mozafari, M. (2018) Nanoengineered  
854 biomaterials for intestine regeneration. *Nanoengineered Biomaterials for Regenerative Medicine*,  
855 pp.363-378.

856

857 Van Tienen, T. G., Heijkants, R. G., Buma, P., de Groot, J. H., Pennings, A. J., & Veth, R. P. (2002).  
858 Tissue ingrowth and degradation of two biodegradable porous polymers with different porosities  
859 and pore sizes. *Biomaterials*, 23(8), 1731-1738.

860

---

861 Wake, M. C., Patrick, C. W., Jr., & Mikos, A. G. (1994). Pore morphology effects on the fibrovascular  
862 tissue growth in porous polymer substrates. *Cell Transplant*, 3(4), 339-343.

863

864 Wang, W., Zhang, P., Zhang, S., Li, F., Yu, J., & Lin, J. (2013). Structure and properties of novel  
865 regenerated cellulose fibers prepared in NaOH complex solution. *Carbohydr Polym*, 98(1), 1031-1038.

866

867 Wanjare, M., Hou, L., Nakayama, K. H., Kim, J. J., Mezak, N. P., & Abilez, O. J. (2017). Anisotropic  
868 microfibrinous scaffolds enhance the organization and function of cardiomyocytes derived from  
869 induced pluripotent stem cells. 5(8), 1567-1578.

870

871 Wu, L., Magaz, A., Wang, T., Liu, C., Darbyshire, A., Loizidou, M., Emberton, M., Birchall, M., & Song,  
872 W. (2018). Stiffness memory of indirectly 3D-printed elastomer nanohybrid regulates  
873 chondrogenesis and osteogenesis of human mesenchymal stem cells. *Biomaterials*, 186, 64-79.

874

875 Yang, G., Li, X., He, Y., Ma, J., Ni, G., & Zhou, S. (2018). From nano to micro to macro: Electrospun  
876 hierarchically structured polymeric fibers for biomedical applications. *Progress in Polymer Science*,  
877 81, 80-113.

878

879 Zarrintaj, P., Bakhshandeh, B., Saeb, M., Sefat, F., Rezaeian, I., Ganjali, M., Ramakrishna, S. and  
880 Mozafari, M. (2018) Oligoaniline-based conductive biomaterials for tissue engineering. *Acta*  
881 *Biomaterialia*, 72, pp.16-34.

882

883 Zhang, C., Xue, X., Luo, Q., Li, Y., Yang, K., Zhuang, X., Jiang, Y., Zhang, J., Liu, J., Zou, G., & Liang, X. J.  
884 (2014). Self-assembled Peptide nanofibers designed as biological enzymes for catalyzing ester  
885 hydrolysis. *ACS Nano*, 8(11), 11715-11723.

886

887 Zhao, J., Lu, C., He, X., Zhang, X., Zhang, W., & Zhang, X. (2015). Polyethylenimine-grafted cellulose  
888 nanofibril aerogels as versatile vehicles for drug delivery. *ACS Appl Mater Interfaces*, 7(4), 2607-2615.

889

890 Zong, H., Xia, X., Liang, Y., Dai, S., Alsaedi, A., Hayat, T., Kong, F., & Pan, J. H. (2018). Designing  
891 function-oriented artificial nanomaterials and membranes via electrospinning and electrospraying  
892 techniques. *Mater Sci Eng C Mater Biol Appl*, 92, 1075-1091.

893